Supplementary Information: Evidence for electronically-driven ferroelectricity in a strongly correlated dimerized BEDT-TTF molecular conductor

Elena Gati, Jonas K.H. Fischer, Peter Lunkenheimer, David Zielke, Sebastian Köhler, Felizitas Kolb, Hans-Albrecht Krug von Nidda, Stephen M. Winter, Harald Schubert, John A. Schlueter, Harald O. Jeschke, Roser Valentí, and Michael Lang

(Dated: May 12, 2018)

I. METHODS - DETAILS

Ab initio calculations: We calculated the bandstructures of κ-(ET)$_2$Hg(SCN)$_2$Cl for the staggered majority conformation of the ethylene endgroups and relaxed all hydrogen positions. All published structures from $T = 10$ K to $T = 296$ K have some degree of ethylene end group disorder, which has significant consequences for the electronic structure[1]. The staggered ethylene end group configuration predominates at all temperatures, with 85% staggered ET molecules at $T = 10$ K, 93% at $T = 50$ K, 84% at $T = 100$ K. At $T = 296$ K, both endgroups are significantly disordered. We also find the structures with staggered ethylene endgroup configuration to be significantly lower in energy. We relaxed all hydrogen positions as they are computed rather than measured in the experimental structures[2]. We extract a tight binding representation of the four bands at the Fermi level[3] (see Supplementary (SI) Fig. 1), considering each ET molecule as a site[4]. We use projective Wannier functions as implemented in FPLO[5].

Single crystal growth: In order to check for sample-to-sample variations, crystals of two different sources were used. Crystals were grown following the procedure reported in Ref. 6. Only for those crystals labeled with #AF087 (#AF093) the following minor modifications were applied: Pure TCE (1,1,2-Trichloroethane) was employed as a solvent with a mixture of Hg(SCN)$_2$ and PPNCl (bis(triphenylphosphoranylidene)ammonium chloride) in a molar ratio of 1:1 serving as the electrolyte. The electrolyte was given in a ten-fold excess to the solution in relation to the ET. A constant current of $0.2\,\mu$A ($0.3\,\mu$A) was applied to platinum electrodes, resulting in a voltage of 0.1 V - 0.3 V. Crystal growth was performed at a temperature of 20 °C and crystals were collected after 4-5 weeks. The crystals used for this work had typical dimensions of $1\,\mathrm{mm}^2 \times 0.35\,\mathrm{mm}$ (#AF087), $0.25\,\mathrm{mm}^2 \times 0.05\,\mathrm{mm}$ (#AF093) and $1\,\mathrm{mm}^2 \times 0.5\,\mathrm{mm}$ (#JAS1721).

Dielectric measurements: For the dielectric measurements, electrodes of graphite paste were applied on either side of the plate-like crystals. Due to the relatively small sample sizes and, hence, small absolute values of the measured capacitances, stray capacitances may lead to an additive contribution in ε', especially in temperature/frequency regions where the intrinsic ε' is small. As the absolute values of ε' are not relevant in the context of the present work, no efforts have been made to correct for this contribution. Additional measurements at high frequencies ($1\,\mathrm{MHz} < \nu < 1\,\mathrm{GHz}$) were performed by a coaxial reflection technique employing an impedance analyzer (Keysight E4991B)[7]. Sample cooling with rates of $\pm\,(0.1$ - $0.4)$ K/min was achieved by a ^{4}He-bath cryostat (Cryovac).

Measurements of relative length change: Measurements of the relative length change $\Delta L_i(T)/L_i = (L_i(T) - L_i(T_0))/L_i(300\,\mathrm{K})$, with L_i being the length along the axis i and T_0 a reference temperature, were performed using a home-built high-resolution capacitive dilatometer. Measurements were performed upon heating and cooling using a rate of $\pm\,1.5$ K/h. Prior to the measurements, the sample was cooled slowly with -3 K/h through the glass-transition region[8] around $T_g \approx 63$ K. Crystals were oriented by eye resulting in a maximum misalignment of 5°.

II. BAND STRUCTURE CALCULATIONS

In Figure 1 we show the evolution of the calculated electronic band structure and density of states with temperature. Note, that 10 K and 50 K structures have been determined based on x-ray measurements at a different instrument; we consider 100 K and 296 K structures more reliable. Therefore, only limited comparison between the two sets of structural data is possible. We find that there is no qualitative change in the electronic structure and Hamiltonian parameters between the original structures and those with equilibrium hydrogen positions.

III. ADDITIONAL DIELECTRIC-SPECTROSCOPY MEASUREMENTS

A. Low-frequency results

Figure 2 shows the temperature dependence of ϵ' of crystal #AF093-1 for additional frequencies as measured by the frequency-response analyzer. No significant frequency dependence is detected.

TABLE I. Tight binding parameters of κ-(BEDT-TTF)$_2$Hg(SCN)$_2$Cl at four different temperatures, calculated with relaxed hydrogen positions and for the majority endgroup configurations.

T (K)	t_1 (meV)	t_2 (meV)	t_3 (meV)	t_4 (meV)	t'/t	U/t
10	117.4	62.7	88.1	42.2	0.840	4.5
50	114.5	63.1	89.5	40.3	0.865	4.4
100	118.9	64.4	89.1	41.6	0.841	4.5
296	126.6	60.0	80.8	42.0	0.792	5.0

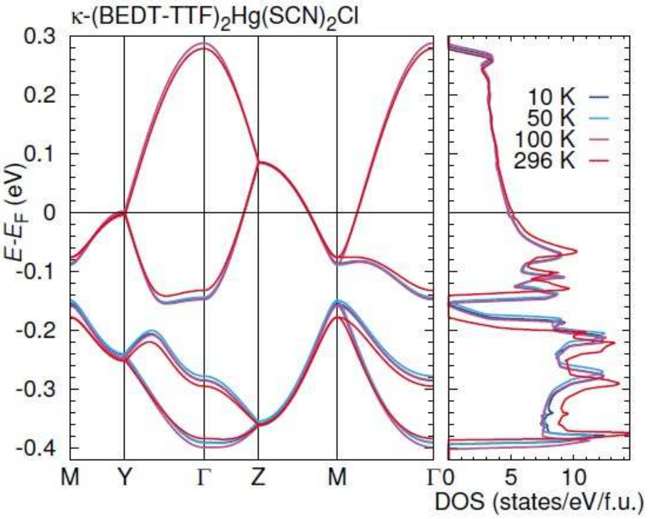

FIG. 1. Band structure of κ-(BEDT-TTF)$_2$Hg(SCN)$_2$Cl at four different temperatures. The majority ethylene endgroup configuration has been chosen in all cases. Note that the underlying structural data at $T = 10$ K and 50 K had been determined based on measurements at a different instrument; we consider the 100 K and 296 K data more reliable.

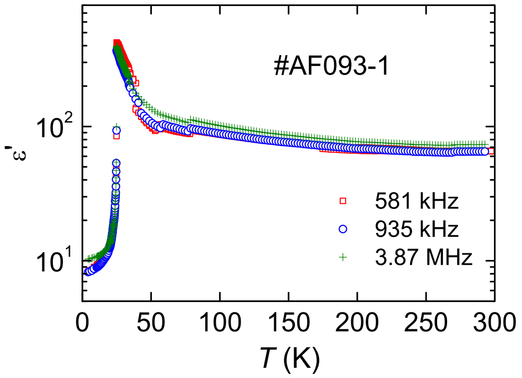

FIG. 2. Temperature dependence of the dielectric constant ϵ' of κ-(BEDT-TTF)$_2$Hg(SCN)$_2$Cl, crystal #AF093-1 measured at three different frequencies.

Figure 3 shows the dielectric constant ε' (a) and conductivity σ' (b) of crystal #JAS1721. The measurements were performed using an autobalance bridge instead of the frequency-response analyzer employed for sample #AF093-1 (Fig. 2 in the main text). Just as for the latter, a well-pronounced asymmetric peak is observed (in this case at 30 K), exhibiting the typical signature of a first-order ferroelectric transition. The peak value of 500 is somewhat higher but of similar order of magnitude as for sample #AF093-1. Its high-temperature flank again can be reasonably well fitted by a Curie-Weiss law with $C = (6300 \pm 1000)$K (dashed line in Fig. 3). In the fitting procedure, T_{CW} was fixed at the same value of 17 K as found for sample #AF093-1. Just as for the latter [Fig. 2(b) in the main text], the conductivity of crystal #JAS1721 [Fig. 3(b)] shows weakly temperature-dependent metal-like behavior above $T_{\mathrm{FE}} = T_{\mathrm{MI}}$ and a sharp drop by several decades below. For this sample this drop reaches almost five orders of magnitude. Apart from the sample-to-sample variation of the electrical properties, the overall behavior of crystals #AF093-1 and #JAS1721 is similar and both show similar signatures of a ferroelectric transition.

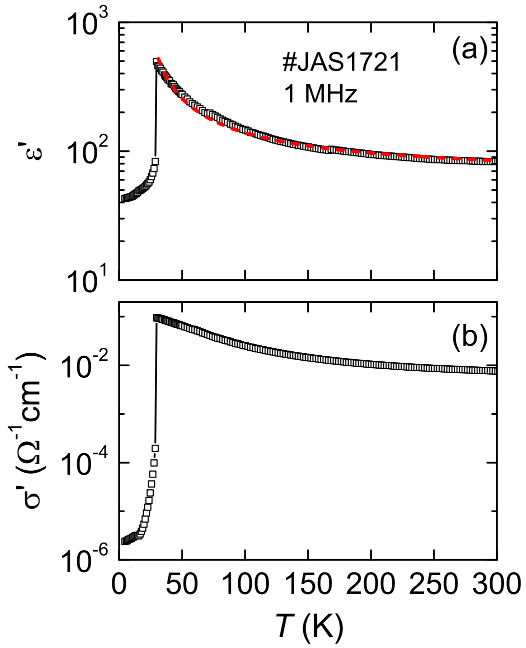

FIG. 3. Temperature dependence of the dielectric constant ε' (a) and conductivity σ' (b) of κ-(BEDT-TTF)$_2$Hg(SCN)$_2$Cl, crystal #JAS1721 measured at 1 MHz. The dashed line has the same meaning as in Fig. 2 of the main text.

B. High-frequency results

Figure 4 shows the temperature-dependent dielectric constant of crystal #AF093-2 at high frequencies, $\nu \geq 4.35\,\mathrm{MHz}$, measured with a coaxial reflection technique using an impedance analyzer[7]. For the lowest frequencies, the typical asymmetric peak, as also detected in the low-frequency measurements of Figs. 2(a) in the main text and 3(a), is revealed (cf. $\varepsilon'(T)$ of crystal #AF093-1 shown by the open circles in Fig. 4). It becomes successively suppressed with increasing frequency. Finally, at the highest frequencies of several hundred MHz, a minimum develops. A similar phenomenon was also observed in other order-disorder ferroelectrics and can be explained by an interplay of the strongly increasing static dielectric constant and the slowing down of the dipolar dynamics when approaching the transition from above T_{FE}[9–11]. An alternative dispersion mechanism was proposed in a recent work[12] which theoretically predicts excitations arising from solitons in quarter-filled molecular solids, however at lower frequencies in the 10 kHz range. When closely inspecting Fig. 4, a small kink is seen at about 25 K, slightly below the peak temperature. This seems to be an artifact as it was only observed in this crystal and may indicate the existence of two sample regions with slightly different T_{FE}.

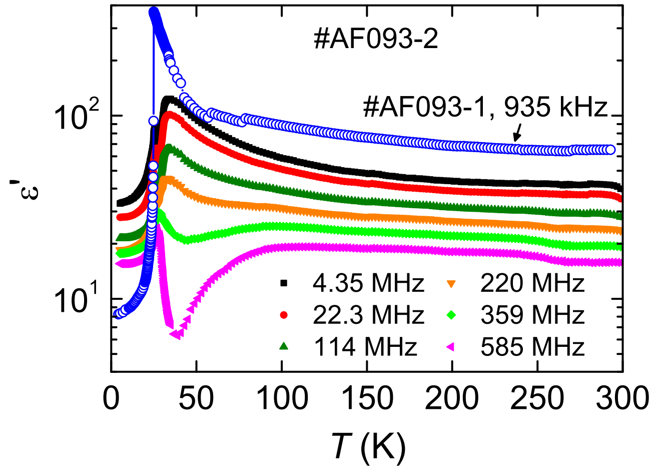

FIG. 4. Temperature dependence of the dielectric constant of κ-(BEDT-TTF)$_2$Hg(SCN)$_2$Cl, crystal #AF093-2, measured for several high frequencies up to 585 MHz (closed symbols). For comparison, the result for crystal #AF093-1 obtained at 935 kHz is shown (open circles).

.

IV. DETERMINATION OF T_{MI} FROM MEASUREMENTS OF THE RELATIVE LENGTH CHANGE $\Delta L_i/L_i$

In order to determine the transition temperature T_{MI} from the data sets of the relative length change $\Delta L_i(T)/L_i$ (see Fig. 3(a) in the main text), we assigned the inflection point of each $\Delta L_i(T)/L_i$ to T_{MI}. This procedure yields slightly different T_{MI} values for the data sets taken along the axes $i = a, b, c$ as already apparent from the bare data. We find $T_{MI,a} = (30.5 \pm 0.1)\,\mathrm{K}$, $T_{MI,b} = (30.0 \pm 0.1)\,\mathrm{K}$ and $T_{MI,c} = (29.8 \pm 0.1)\,\mathrm{K}$. This small discrepancy can be assigned to the influence of the small uniaxial pressure exerted by the dilatometer when mounting the crystal. The corresponding force (typically less than 1 N) is caused by the flat springs[13] which suspend the upper plate of the capacitor in the dilatometer cell. For the present crystal of dimensions $0.25 \times 1.1 \times 0.9\,\mathrm{mm}^3$, the corresponding uniaxial pressure components P_i amount to $P_a \approx 0.6\,\mathrm{MPa}$ and $P_b \approx P_c \approx 2\,\mathrm{MPa}$. As deduced from the different signs in the expansion $\Delta L_i/L_i|_{T_{MI}}$ (see Fig. 3, main text), the uniaxial pressure dependence of T_{MI} is positive for uniaxial pressure along the out-of-plane a axis and negative for the other two directions. Correspondingly, as a result of the uniaxial pressure acting on the crystal along the measuring direction, we find a value for $T_{MI,a}$ which is slightly larger than those of $T_{MI,b}$ and $T_{MI,c}$. In addition, using the criterion defined above, we can quantify the hysteresis presented in Fig. 3 (b) in the main text. We find a difference in the transition temperature determined from data sets taken upon warming and cooling of $\Delta T_{MI} = (0.3 \pm 0.1)\,\mathrm{K}$.

V. ENTROPY RELEASE AT THE CHARGE-ORDER METAL-INSULATOR TRANSITION

In the following, we estimate the entropy release at the charge-order metal-insulator transition at T_{MI} by using results from specific heat $C(T)$ and the relative length change $\Delta L_i(T)/L_i$.

A. Specific heat - Experimental details

Measurements of specific heat were performed by employing a high-resolution ac-modulation technique[14] on a single crystal from batch #AF087-3 of mass $m = (75 \pm 20)\,\mu\mathrm{g}$. Details of the setup, specially designed for measuring small plate-like crystals, are presented in Ref. 15. Measurements were performed upon warming in the range $2\,\mathrm{K} \leq T \leq 35\,\mathrm{K}$.

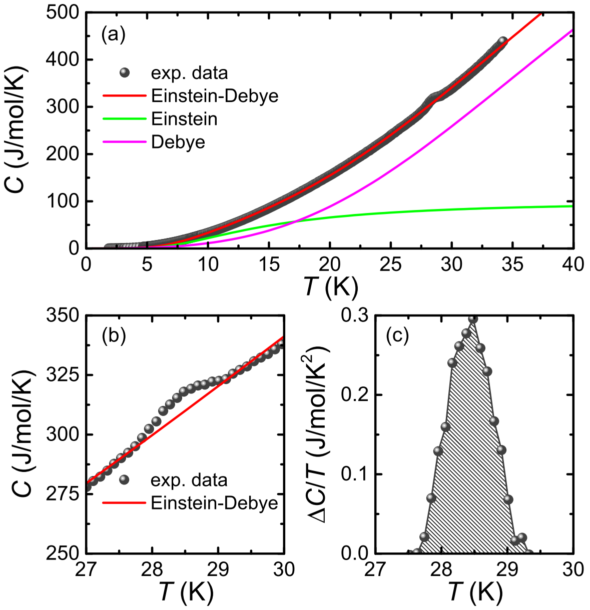

FIG. 5. Specific heat C of κ-(BEDT-TTF)$_2$Hg(SCN)$_2$Cl: (a) experimental data of C vs. T (grey circles) in the range $2\,\mathrm{K} \leq T \leq 35\,\mathrm{K}$. Red line corresponds to a fit of the phononic background contribution C_{Ph} which is described by a sum of an Einstein (green line) and a Debye contribution (pink line); (b) Anomaly, visible in the C vs. T data at $T \approx 28.5\,\mathrm{K}$ on expanded scales and the phononic background fit (Einstein-Debye fit); (c) Plot of $\Delta C/T = (C - C_{Ph})/T$ vs. T. The shaded area corresponds to the entropy change ΔS at the phase transition.

B. Specific heat - Results

Figure 5 (a) shows data of C vs. T in the temperature range $2\,\mathrm{K} \leq T \leq 35\,\mathrm{K}$. We observe an overall increase of C with increasing T with a small hump around $T \approx 28.5\,\mathrm{K}$. We assign this feature, which is shown on an enlarged scale in Fig. 5 (b), to the signature of the metal-insulator transition at T_{MI}. Note that we have provided experimental evidence from measurements of the relative length change $\Delta L_i/L_i$ (see main text, Fig. 3) that this phase transition is of first-order. Consequently, a divergence in $C(T)$ at T_{MI} would be expected. However, due to the ac-technique applied here, which involves temperature oscillations with typical amplitudes $\Delta T/T \sim 0.01$, sharp features can become smeared out or rounded.

In order to determine the entropy release ΔS associated with the phase transition, we have to subtract all other contributions to C which evidently dominate the overall behavior of $C(T)$. As the sample is insulating for $T \leq 30\,\mathrm{K}$, electronic contributions can be neglected in this temperature regime and C is assumed to be given solely by phonon contributions C_{Ph}. For the description of C_{Ph}, we employ a model in which we take Debye- and Einstein-type of oscillations into account. Whereas the former ones account well for the contribution of acoustic phonons with an, in first approximation, linear dispersion close to the Brillouin zone center, the latter one describes the contribution of optical phonons with a small dispersion. The resulting model reads as

$$C_{Ph}(T) = 9N_D R \left(\frac{T}{\Theta_D}\right)^3 \int_0^{\Theta_D/T} x^4 \frac{e^x}{(e^x-1)^2}\,\mathrm{d}x + 3N_E R \left(\frac{\Theta_E}{T}\right)^2 \frac{e^{\Theta_E/T}}{(e^{\Theta_E/T}-1)^2}, \quad (1)$$

with N_D (N_E) the number of Debye (Einstein) oscillators and Θ_D (Θ_E) the Debye (Einstein) temperature. The significant contribution of optical phonons even at such low temperatures in the present case can be inferred from a plot of C/T^3 vs. T. In this representation, Debye contributions, which follow $C_{Debye} \propto T^3$ at low temperatures, give rise to a horizontal line, whereas Einstein contributions show a pronounced maximum. Such a maximum can be observed for the present data set at $T \approx 6.6\,\mathrm{K}$ reflecting the presence of low-lying optical phonons. These two dominant contributions to $C(T)$ were also identified for other charge-transfer salts, such as κ-(ET)$_2$I$_3$[16]. The low-lying optical phonons were often assigned to librational modes[16] of the anion motion[17,18].

The model contains three free parameters, namely N_E, Θ_D and Θ_E, as we keep the total number of oscillators $N = N_D + N_E$ fixed and equate it with the number of molecules per formula unit, $N = 60$. The obtained fit, which is in very good agreement with the data set for $T < 27.5\,\mathrm{K}$, is shown in Fig. 5 (a) and (b) by the red line. The resulting fit parameters amount to $\Theta_D = (210 \pm 20)\,\mathrm{K}$, $\Theta_E = (46 \pm 5)\,\mathrm{K}$ and $N_E = 4$. The Debye temperature obtained here is in good agreement with those determined for other charge-transfer salts[16,19–21] which typically range from 180 K to 220 K. Also Θ_E is similar to values found, e.g., for κ-(ET)$_2$I$_3$, the specific heat[16] of which was modeled with $N_E = 2$ oscillators. The values determined here therefore confirm the reliability of our fit.

After we determined the background, we can now proceed with analyzing the specific heat and the entropy associated with the phase transition. To this end, we evaluate $\Delta C(T)/T = (C(T) - C_{Ph}(T))/T$ (see Fig. 5 (c)). The integration of $\Delta C(T)/T$ in the temperature range from 27.5 K to 29.5 K (shaded area in Fig. 5 (c)) yields $\Delta S = (250 \pm 50)\,\mathrm{mJ\,mol^{-1}K^{-1}}$.

C. Clausius-Clapeyron equation - Results

In the previous section, we presented the determination of the entropy change ΔS across the first-order phase transition at T_{MI} from specific heat measurements. In this paragraph, we present a second, independent approach to ΔS by using the Clausius-Clapeyron equation $\mathrm{d}T_{MI}/\mathrm{d}P = \Delta V/\Delta S$ and the experimentally determined quantities ΔV and $\mathrm{d}T_{MI}/\mathrm{d}P$. To this end, we determined the volume jump[22] at the metal-insulator transition $\Delta V/V|_{T_{MI}}$ from the present $\Delta L_i/L_i$ data by $\Delta V/V|_{T_{MI}} \simeq \sum_i \Delta L_i/L_i|_{T_{MI}}$ with $i = a, b, c$. The individual $\Delta L_i/L_i|_{T_{MI}}$ contributions were determined using the following procedure (as indicated exemplarily for the c axis data by the dotted lines in Fig. 3 (a), main text): The slightly broadened jumps in $\Delta L_i/L_i$ were replaced by infinitely sharp jumps by extrapolating the normal background from both sides of the transition up to T_{MI}. The resulting relative length changes at T_{MI} amount to $\Delta L_a/L_a|_{T_{MI}} = (1.45 \pm 0.05) \cdot 10^{-4}$, $\Delta L_b/L_b|_{T_{MI}} = -(1.60 \pm 0.05) \cdot 10^{-4}$ and $\Delta L_c/L_c|_{T_{MI}} = (1.65 \pm 0.05) \cdot 10^{-4}$ and, accordingly, $\Delta V/V|_{T_{MI}} = -(1.80 \pm 0.15) \cdot 10^{-4}$. Note that a relative volume change of similar size has been revealed at the Mott metal-insulator transition for κ-(ET)$_2$Cu[N(CN)$_2$]Cl[23]. Together with the molar volume of $V_{mol} = 5.36 \cdot 10^{-4}\,\mathrm{m}^3/\mathrm{mol}$ and $\mathrm{d}T_{MI}/\mathrm{d}P \approx -(0.33 \pm 0.03)\,\mathrm{K/MPa}$ determined experimentally (see Fig. 8) on a crystal from the same batch, the entropy change can be determined as $\Delta S = (290 \pm 30)\,\mathrm{mJ\,mol^{-1}\,K^{-1}}$. This value of ΔS is, within the error bars, consistent with the value given in the previous section.

D. Discussion

Given that the metal-insulator transition is a first-order transition involving only charge degrees of freedom, an entropy change of $\Delta S = \gamma T_{MI}$, with γ being the electronic Sommerfeld coefficient, would be expected. Under this assumption, the experimentally determined ΔS, gives $\gamma \simeq 10\,\mathrm{mJ\,mol^{-1}\,K^{-2}}$. This value of γ is at the lower bound of γ values found for other organic charge-transfer salts[16,19–21,24] which typically are in the range $10\,\mathrm{mJ\,mol^{-1}\,K^{-2}} \lesssim \gamma \lesssim 30\,\mathrm{mJ\,mol^{-1}\,K^{-2}}$. The comparably low γ value determined here is in agreement with the somewhat weaker correlations, predicted by our DFT calculations, which results in a smaller effective mass. Thus, the present result of the entropy change ΔS can be explained consistently by considering only the effect of charge degrees of freedom. We infer that, if present at all, any change of a magnetic entropy at T_{MI} would be very small.

VI. ESR MEASUREMENTS

A. Experimental details

Electron spin resonance (ESR) measurements have been performed in a Bruker ELEXSYS E500 spectrometer working at X– ($\nu = 9.34$ GHz) and Q-band frequencies ($\nu = 34$ GHz) with *Oxford* He-gas flow cryostats ESR 900 and ESR 935 covering the temperature range $4\,\mathrm{K} \leq T \leq 300\,\mathrm{K}$. The single crystals were fixed in high-purity *Suprasil* quartz-glass tubes by paraffin and mounted in the microwave cavity. A goniometer is used to adjust the orientation of the sample in the external static magnetic field H. ESR measures the microwave absorption from magnetic dipolar transitions excited by the transverse magnetic microwave field between the electronic Zeeman levels dependent on the static magnetic field. Resonance occurs if the microwave energy matches the Zeeman splitting, i.e., $h\nu = g\mu_B H$, where h denotes the Planck constant, μ_B the Bohr magneton and g is the g value. Due to the lock-in technique with field modulation the field derivative $\mathrm{d}P/\mathrm{d}H$ of the absorbed microwave power is recorded.

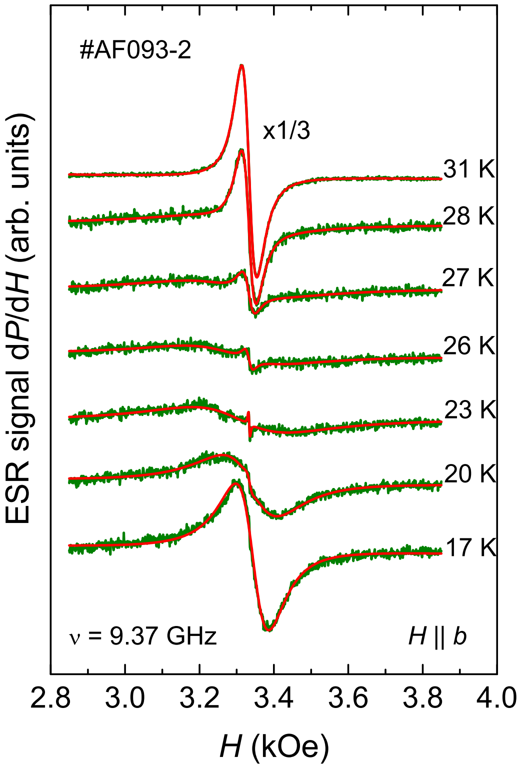

FIG. 6. Selected ESR spectra of κ-(BEDT-TTF)$_2$Hg(SCN)$_2$Cl #AF093-2 for the magnetic field applied along the crystallographic b axis. The red solid lines correspond to fits with one or two Lorentz lines as discussed in the text.

B. Results

Figure 6 shows typical ESR spectra of κ-(ET)$_2$Hg(SCN)$_2$Cl on crossing the MI transition. At temperatures above T_{MI} the ESR spectrum consists of a single absorption line at a g value close to the free electron value $g = 2.0023$, typical for conduction electrons. The line shape depends on the orientation of the magnetic microwave field with respect to the conducting bc layers. If the magnetic microwave field

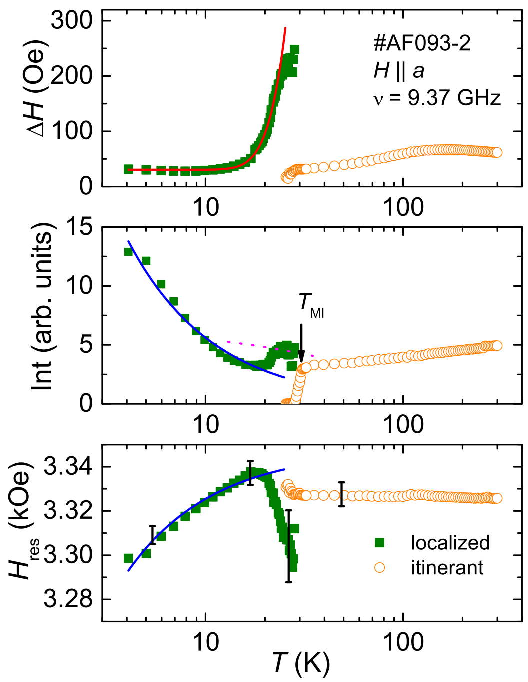

FIG. 7. Temperature dependence of linewidth ΔH (top), intensity (middle), and resonance field H_{res} (bottom) of κ-(BEDT-TTF)$_2$Hg(SCN)$_2$Cl #AF093-2 for the magnetic field applied along the crystallographic a axis. The red solid line in the top frame indicates a fit by an Arrhenius law with an energy gap of $\Delta/k_B \approx 130$ K, the blue solid lines in middle and bottom frame indicate pure Curie-Weiss laws while the magenta dotted line represents a Curie-Weiss (CW) law with a CW temperature of $\Theta_{CW} = -60$ K.

oscillates within the bc plane one observes a pure Lorentz line, while it becomes asymmetric when the magnetic microwave field oscillates perpendicular to the bc plane (not shown). In the latter case strong shielding currents are induced into the conducting planes (skin effect) leading to an admixture of dispersion into the absorption signal.[25] Hence, in general the ESR signals are fitted by the field derivative of the expression

$$P(H) = A\frac{\Delta H + \alpha(H - H_{res})}{(H - H_{res})^2 + \Delta H^2} \tag{2}$$

with the amplitude A, resonance field H_{res}, line width ΔH and dispersion-to-absorption ratio α. For high conductivity $\alpha \to 1$ is approached, while for low conductivity ($\alpha \to 0$) the signal corresponds to a pure Lorentz line. This is the case, if the magnetic microwave field is applied within the bc-plane: then the shielding currents are cut along the a-direction, thus the skin effect can be neglected. Below T_{MI} a second much broader line shows up. While the first line strongly weakens on further decreasing temperature, the second one strengthens and narrows and finally becomes dominant below 20 K.

Figure 7 exemplarily illustrates the temperature dependence of linewidth, intensity, and resonance field of both signals for the magnetic field applied along the crystallographic a axis. The linewidth of the first line starts at a value of about 70 Oe at room temperature, narrows below 150 K on approaching the MI transition, below which it decreases further. Concomitantly, the second line shows up with a much broader linewidth of about 250 Oe, but strongly narrows below 20 K following an Arrhenius law with an energy gap $\Delta/k_B \approx 130$ K, and finally reaches a value of about 30 Oe at low temperatures. The (with respect to the field derivative $\mathrm{d}P/\mathrm{d}H$) double-integrated intensity $I \propto A\Delta H^2$ monotonously decreases with decreasing temperature down to the MI transition, below which it abruptly decreases, while the second line clearly gains intensity, decreases abruptly at 20 K and finally increases down to lowest temperature. Note that the regime between 20 and 30 K can be approximated by a Curie-Weiss law with CW temperature of about -60 K, while below 15 K a pure Curie law best approximates the data. The resonance field is temperature independent at $g_a = 2.013$ above T_{MI}. To lower temperatures the second broad line appears at $g \approx 2.03$ shifts slightly below 2.01 at 20 K and returns on further cooling approximately following a Curie law like the intensity. At 4 K one finds $g_a(T = 4\text{ K}) \approx 2.03$.

For $H||b$ and $H||c$ (not shown) the temperature dependence of linewidth and intensity is very similar to that for $H||a$. The high-temperature g values are found at $g_b = 2.009$ and $g_c = 2.006$. Regarding low temperatures, the resonance field decreases on approaching 4 K for $H||b$ ($g_b(T = 4\text{ K}) = 2.04$) but increases for $H||c$ ($g_c(T = 4\text{ K}) = 1.95$). Comparative ESR measurements at Q-band frequency did not reveal any significant differences to the X-band results and will not be discussed further here.

Our ESR results are in general agreement with the data reported by Yasin *et al.*[26] The temperature dependence of linewidth, intensity, and resonance fields is comparable to our findings and reveals anomalies at T_{MI} and around 20 K as well. At high temperatures the anisotropy of the g tensor $g_a > g_b > g_c$ is the same, only the absolute values are slightly higher (by $\Delta g \approx 0.003$) in our case. Also the evolution of the anisotropy down to $T = 4$ K is comparable to the earlier work. However, our detailed measurements employing small temperature steps around the MI transition revealed the separation of the ESR signal into two different lines below T_{MI} which has not been reported before. This clearly indicates the onset of localization of the conduction electrons at T_{MI}: the narrow line coming from high temperatures belongs to the itinerant electrons, while the broad line appearing below 30 K arises from the localized electrons.

The ESR intensity of the narrow line increases with increasing temperature as characteristic for the spin susceptibility of an antiferromagnetically coupled two-dimensional metallic electron system, like e.g. in iron pnictides[27]. The intensity of the contribution associated to the localized electrons reveals a weak increase upon cooling down to 20 K. This behavior would be compatible with a Curie-Weiss law between T_{MI} and 20 K. Our calibration measurements prove that roughly one electron spin per formula unit contributes to the susceptibility in this temperature range. Hence the spin system behaves like a paramagnet of antiferromagnetically exchange-coupled localized spins. The g value exhibits a significant shift from the conduction-electron value at T_{MI} indicating the change of local fields during the localization process. At the same time the linewidth is rather broad probably due to strong charge and spin fluctuations. Below 25 K the exponential decrease of the linewidth indicates the stabilization of charge order in agreement with the steep decrease of the dielectric constant. We note that the determined gap size $\Delta/k_B = 130\,\mathrm{K}$ is consistent with the charge gap determined by optical measurements[2]. A similar linewidth behavior was observed in β-$\mathrm{Na}_{1/3}\mathrm{V}_2\mathrm{O}_5$ below the metal-to-insulator transition in the charge ordered phase, where the temperature dependence of the linewidth could be clearly related to the conductivity[28]. Finally, the reason for the Curie-like behavior of intensity and resonance shift below 15 K has to be addressed: Here only approximately 20% of the spins seem to contribute. Regarding the anisotropy at 4 K, Yasin *et al.*[26] proposed some kind of antiferromagnetic order like in the related copper compound κ-$(\mathrm{ET})_2\mathrm{Cu}[\mathrm{N}(\mathrm{CN})_2]\mathrm{Cl}$. However, the anisotropy is by far smaller in the present compound and proportional to the spin susceptibility, i.e., the resonance shift originates from the internal field due to the magnetization of the sample. There are similarities to the behavior in κ-$(\mathrm{ET})_2\mathrm{Hg}(\mathrm{SCN})_2\mathrm{Br}$, which exhibits weakly ferromagnetic spin-glass type properties at low temperatures due to frustration and disorder.[29] Note, however that there is no charge order in the Br compound and the anisotropy is only similar in the absolute value, but its orientation with respect to the crystallographic axes is different. Hence, with the present data a final conclusion about the magnetic ground state is not possible, but long-range antiferromagnetic order seems to be very unlikely.

VII. RESISTIVITY UNDER PRESSURE

A. Experimental details

The electrical resistivity ρ was measured in a standard four-terminal configuration using a DC current $I = 1\,\mu\mathrm{A}$. The current was applied within the bc plane using a HP3245A universal source. The voltage was read out by a Keithley 2182A nanovoltmeter. Carbon paste (Jeol Datum Ltd., Japan) was used to attach contacts to the crystals. Measurements under finite pressure were performed up to pressures of 300 MPa. To this end, the sample was placed in a CuBe pressure cell (Institute of High-Pressure Physics, Polish Academy of Sciences, Unipress Equipment Division) that was connected to a He-gas compressor via a capillary. The large volume of the compressor which is kept at room temperature ensures $P \simeq$ const. conditions during a T-sweep with $\Delta P = \pm 1\,\mathrm{MPa}$. Helium gas was used as a pressure-transmitting medium to ensure a hydrostatic pressure environment to lowest temperatures which is of particular importance in the study of organic charge-transfer salts. These systems usually exhibit strong and anisotropic uniaxial pressure coefficients[30] which make them sensitive to non-hydrostatic pressure components. Pressure was determined *in-situ* by an n-InSb sensor[31]. Measurements were performed upon warming using a rate of $+7.2\,\mathrm{K/h}$.

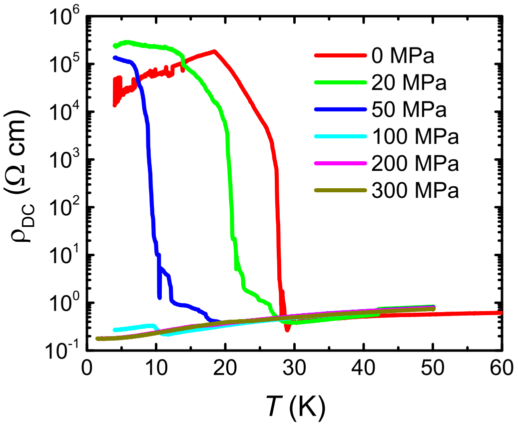

FIG. 8. Resistivity ρ of κ-(BEDT-TTF)$_2$Hg(SCN)$_2$Cl (crystal #AF087-2) as a function of temperature T under various external pressures ($0\,\mathrm{MPa} \leq P \leq 300\,\mathrm{MPa}$). Pressure values given in the legend were measured at high temperatures, i.e., 60 K. Note that the pressure medium ^{4}He solidifies under P at low T which is accompanied by a pressure loss. This results in small jumps in the data sets taken at 100 MPa, 200 MPa and 300 MPa.

B. Results

First, we focus on the investigation of the properties of the charge-order MI transition. Figure 8 shows the resistivity $\rho(T)$ of a crystal of κ-$(\mathrm{ET})_2\mathrm{Hg}(\mathrm{SCN})_2\mathrm{Cl}$ at ambient pressure as well as finite pressures up to 300 MPa. We note that pressure studies on this compound were reported in literature[32]. However, this study is the first one that is conducted under truly hydrostatic pressure conditions - an aspect which is of high importance whenever a phase transition is accompanied by strong and anisotropic length changes. The latter is the case for the present compound, as we will demonstrate below in more detail.

At ambient pressure the MI transition manifests itself in a sharp increase in $\rho(T)$ by 3 to 4 orders of magnitude upon cooling below at $T_{MI} \approx 29\,\mathrm{K}$, followed by a shoulder and a less rapid increase at slightly lower temperatures, as similarly reported in Refs. 26, 32. With increasing pressure, the transition temperature becomes rapidly suppressed to lower temperatures while a broad tail, composed of several small steps, develops at the high-temperature end of the transition. Since in this temperature-pressure range the pressure-transmitting medium helium is still in its liquid phase, we can rule out that this broadening is due to non-hydrostatic pressure conditions. By assigning the transition temperature T_{MI} to the point where $\mathrm{d}\log\rho(T)/\mathrm{d}T$ becomes maximum, we find an initial rate of $\mathrm{d}T_{MI}/\mathrm{d}P \approx -(0.33 \pm 0.03)\,\mathrm{K/MPa}$. This value is consistent with the pressure dependence of T_{MI} revealed from resistivity measurements by using oil as a pressure-transmitting medium, although there the broadening of the transition at finite pressure was distinctly more pronounced[32].

At a pressure of 100 MPa, the data do not reveal any signature of a MI transition and the system remains metallic down to the lowest temperature of our experiment of $T = 2\,\mathrm{K}$. Note that the small step-like increase of the resistivity below about 10 K is due to the solidification of helium which is accompanied by a pressure loss from 100 MPa to about 65 MPa. We find that the metallic state which evolves at low temperature does not change much upon further increasing the pressure. Especially, there are no indications for superconductivity up to 300 MPa for $T > 2\,\mathrm{K}$. Such an insensitivity of the metallic state to pressure changes and the lack of pressure-induced superconductivity are in marked contrast to those κ-$(\mathrm{ET})_2X$ salts which are located close to the Mott transition P[33–36].

---

[1] D. Guterding, R. Valentí, and H. O. Jeschke, Phys. Rev. B **92**, 081109 (2015).

[2] N. Drichko, R. Beyer, E. Rose, M. Dressel, J. A. Schlueter, S. A. Turunova, E. I. Zhilyaeva, and R. N. Lyubovskaya, Phys. Rev. B **89**, 075133 (2014).

[3] H. C. Kandpal, I. Opahle, Y.-Z. Zhang, H. O. Jeschke, and R. Valentí, Phys. Rev. Lett. **103**, 067004 (2009).

[4] M. Altmeyer, R. Valentí, and H. O. Jeschke, Phys. Rev. B **91**, 245137 (2015).

[5] H. Eschrig and K. Koepernik, Phys. Rev. B **80**, 104503 (2009).

[6] S. V. Konovalikhin, G. V. Shilov, O. A. D'yachenko, R. N. Lyubovskaya, M. Z. Aldoshina, and R. B. Lyubovskii, Bulletin of the Russian Academy of Sciences, Division of chemical science **41**, 704 (1992), ISSN 1573-9171.

[7] R. Böhmer, M. Maglione, P. Lunkenheimer, and A. Loidl, J. Appl. Phys. **65**, 901 (1989).

[8] E. Gati, S. M. Winter, J. A. Schlueter, H. Schubert, J. Müller, and M. Lang, Phys. Rev. B **97**, 075115 (2018).

[9] R. Blinc and B. Žekš, *Soft Modes in Ferroelectrics and Antiferroelectrics* (North-Holland, Amsterdam, 1994).

[10] F. Sandy and R. V. Jones, Phys. Rev. **168**, 481 (1968).

[11] Y. Takayama, K. Deguchi, and E. Nakamura, J. Phys. Soc. Jpn. **53**, 4121 (1984).

[12] H. Fukuyama, J. Kishine, and M. Ogata, J. Phys. Soc. Jpn. **86**, 123706 (2017).

[13] R. Pott and R. Schefzyk, J. Phys. E: Sci. Instrum. **16**, 444 (1983).

[14] P. F. Sullivan and G. Seidel, Phys. Rev. **173**, 679 (1968).

[15] J. Müller, M. Lang, R. Helfrich, F. Steglich, and T. Sasaki, Phys. Rev. B **65**, 140509 (2002).

[16] J. Wosnitza, X. Liu, D. Schweitzer, and H. J. Keller, Phys. Rev. B **50**, 12747 (1994).

[17] P. Foury-Leylekian, S. Petit, I. Mirebeau, G. André, M. de Souza, M. Lang, E. Ressouche, A. Moradpour, and J.-P. Pouget, Phys. Rev. B **88**, 024105 (2013).

[18] R. Świetlik, H. Grimm, D. Schweitzer, and H. J. Keller, Z. Naturforsch. A **42**, 603 (1987).

[19] B. Andraka, G. R. Stewart, K. D. Carlson, H. H. Wang, M. D. Vashon, and J. M. Williams, Phys. Rev. B **42**, 9963 (1990).

[20] B. Andraka, J. S. Kim, G. R. Stewart, K. D. Carlson, H. H. Wang, and J. M. Williams, Phys. Rev. B **40**, 11345 (1989).

[21] S. Katsumoto, S. ichi Kobayashi, H. Urayama, H. Yamochi, and G. Saito, J. Phys. Soc. Jpn. **57**, 3672 (1988).

[22] Note that we neglect here a small correction that arises from the monoclinic $\beta = 91^\circ$ angle[2].

[23] E. Gati, M. Garst, R. S. Manna, U. Tutsch, B. Wolf, L. Bartosch, H. Schubert, T. Sasaki, J. A. Schlueter, and M. Lang, Science Advances **2** (2016).

[24] P. Garoche, R. Brusetti, D. Jérome, and K. Bechgaard, J. Physique Lett. **43**, 147 (1982).

[25] S. Barnes, Adv. Phys. **30**, 801 (1981).

[26] S. Yasin, E. Rose, M. Dumm, N. Drichko, M. Dressel, J. Schlueter, E. Zhilyaeva, S. Torunova, and R. Lyubovskaya, Physica B: Cond. Mat. **407**, 1689 (2012), ISSN 0921-4526.

[27] R. Jin, M. H. Pan, X. B. He, G. Li, D. Li, R. wen Peng, J. R. Thompson, B. C. Sales, A. S. Sefat, M. A. McGuire, et al., Supercond. Sci. Technol. **23**, 054005 (2010).

[28] M. Heinrich, H.-A. Krug von Nidda, R. M. Eremina, A. Loidl, C. Helbig, G. Obermeier, and S. Horn, Phys. Rev. Lett. **93**, 116402 (2004).

[29] M. Hemmida, H.-A. Krug von Nidda, B. Miksch, L. L. Samoilenko, A. Pustogow, J. Schlueter, A. Loidl, and M. Dressel, arXiv:1710.04028 [cond-mat.str-el] (2017).

[30] J. Müller, M. Lang, F. Steglich, J. A. Schlueter, A. M. Kini, U. Geiser, J. Mohtasham, R. W. Winter, G. L. Gard, T. Sasaki, et al., Phys. Rev. B **61**, 11739 (2000).

[31] W. Kraak, U. Schaller, and R. Herrmann, physica status solidi (a) **85**, K183 (1984), ISSN 1521-396X.

[32] A. Löhle, E. Rose, S. Singh, R. Beyer, E. Tafra, T. Ivek, E. I. Zhilyaeva, R. N. Lyubovskaya, and M. Dressel, J. Phys.: Condens. Matter **29**, 055601 (2017).

[33] Y. Kurosaki, Y. Shimizu, K. Miyagawa, K. Kanoda, and G. Saito, Phys. Rev. Lett. **95**, 177001 (2005).

[34] P. Limelette, P. Wzietek, S. Florens, A. Georges, T. A. Costi, C. Pasquier, D. Jérome, C. Mézière, and P. Batail, Phys. Rev. Lett. **91**, 016401 (2003).

[35] S. Lefebvre, P. Wzietek, S. Brown, C. Bourbonnais, D. Jérome, C. Mézière, M. Fourmigué, and P. Batail, Phys. Rev. Lett. **85**, 5420 (2000).

[36] C. Strack, C. Akinci, V. Pashchenko, B. Wolf, E. Uhrig, W. Assmus, M. Lang, J. Schreuer, L. Wiehl, J. A. Schlueter, et al., Phys. Rev. B **72**, 054511 (2005).